



HAL
open science

Parallel on-chip micropipettes enabling quantitative multiplexed characterization of vesicle mechanics and cell aggregates rheology

Sylvain Landiech, Marianne Elias, Pierre Lapèze, Hajar Ajiyel, Marine Plancke, Blanca González-Bermúdez, Adrian Laborde, Fabien Mesnilgrete, David Bourrier, Debora Berti, et al.

► To cite this version:

Sylvain Landiech, Marianne Elias, Pierre Lapèze, Hajar Ajiyel, Marine Plancke, et al.. Parallel on-chip micropipettes enabling quantitative multiplexed characterization of vesicle mechanics and cell aggregates rheology. *APL Bioengineering*, 2024, 8 (2), pp.026122. 10.1063/5.0193333 . hal-04616249

HAL Id: hal-04616249

<https://hal.science/hal-04616249>

Submitted on 18 Jun 2024

HAL is a multi-disciplinary open access archive for the deposit and dissemination of scientific research documents, whether they are published or not. The documents may come from teaching and research institutions in France or abroad, or from public or private research centers.

L'archive ouverte pluridisciplinaire **HAL**, est destinée au dépôt et à la diffusion de documents scientifiques de niveau recherche, publiés ou non, émanant des établissements d'enseignement et de recherche français ou étrangers, des laboratoires publics ou privés.



Distributed under a Creative Commons Attribution - NonCommercial 4.0 International License

This is the author's peer reviewed, accepted manuscript. However, the online version of record will be different from this version once it has been copyedited and typeset.

PLEASE CITE THIS ARTICLE AS DOI: 10.1063/1.5019333

1 **Parallel on-chip micropipettes enabling quantitative multiplexed**
 2 **characterization of vesicle mechanics and cell aggregates rheology**

3 Sylvain Landiech^{1†}, Marianne Elias^{1†}, Pierre Lapèze¹, Hajar Ajiye¹, Marine Plancke¹, Blanca
 4 González-Bermúdez², Adrian Laborde¹, Fabien Mesnilgrete¹, David Bourrier¹, Debora Berti³,
 5 Costanza Montis³, Laurent Mazon¹, Jérémy Baldo¹, Clément Roux⁴, Morgan Delarue¹, Pierre
 6 Joseph^{1*}

7 [†]These two authors contributed equally.

8 *Corresponding author pierre.joseph@laas.fr

9 **Affiliations**

10 ¹ LAAS-CNRS, Université de Toulouse, CNRS, Toulouse, France

11 ² Center for Biomedical Technology, Universidad Politécnica de Madrid, Pozuelo de Alarcón,
 12 Spain and Department of Materials Science, ETSI de Caminos, Canales y Puertos, Universidad
 13 Politécnica de Madrid, Madrid, Spain

14 ³ CSGI and Department of Chemistry, University of Florence, Sesto Fiorentino, Italy

15 ⁴ SoftMat, Université de Toulouse, CNRS, UPS, Toulouse, France

16

17 **Abstract**

18 Micropipette aspiration (MPA) is one of the gold standards for quantifying biological samples'
 19 mechanical properties, which are crucial from the cell membrane scale to the multicellular
 20 tissue. However, relying on the manipulation of individual home-made glass pipettes, MPA
 21 suffers from low throughput and no automation. Here, we introduce the sliding insert
 22 micropipette aspiration (SIMPA) method, which permits parallelization and automation, thanks
 23 to the insertion of tubular pipettes, obtained by photolithography, within microfluidic channels.
 24 We show its application both at the lipid bilayer level, by probing vesicles to measure
 25 membrane bending and stretching moduli, and at the tissue level by quantifying the
 26 viscoelasticity of 3D cell aggregates. This approach opens the way to high-throughput,
 27 quantitative mechanical testing of many types of biological samples, from vesicles and
 28 individual cells to cell aggregates and explants, under dynamic physico-chemical stimuli.

29

30 **Introduction**

31 Mechanics is ubiquitously at play in biology, from the level of cell membranes to the tissue
 32 scale. At the cell scale, response to stimuli is related to its cytoskeleton and nucleus but also
 33 strongly depends upon the deformability of its membrane¹. At the multicellular scale, the
 34 capacity of cell assemblies to deform and flow is a determining factor in tissue homeostasis and
 35 evolution. This idea applies to developmental biology, since embryo morphogenesis is strongly
 36 intertwined with spatiotemporal changes and heterogeneity in fluidity^{2,3}. It is also an essential
 37 ingredient for pathological situations such as solid cancers: the ability of cells to deform and
 38 spread, or jam, is key in disease progression⁴. Tissue rheology can thus be envisioned as a
 39 diagnostics tool⁵, or even to assist the prognosis of metastasis⁶.

40 Thus, strong efforts have been made in the last decades to engineer quantitative tools assessing
 41 mechanical properties of cell membranes⁷, cells⁸, and cell aggregates⁹, often relying on

This is the author's peer reviewed, accepted manuscript. However, the online version of record will be different from this version once it has been copyedited and typeset.

PLEASE CITE THIS ARTICLE AS DOI: 10.1063/1.5019333

42 analogies with soft matter as proposed in Steinberg's pioneering work¹⁰, and on concepts of
43 rheology¹¹. One popular technique is micropipette aspiration MPA¹²⁻¹⁴, both at cell and tissue
44 scale. MPA measures to what extent a vesicle, a cell, or a tissue enters a glass tube upon
45 aspiration. It permits quantifying: bending and stretching rigidity for lipid vesicles mimicking
46 cell membranes; apparent Young's modulus and effective viscosity for single cells⁸; surface
47 tension, elasticity and viscosity for 3D cell aggregates¹⁵. MPA is one of the gold standards
48 because it is quantitative, and it probes locally a zone that can be chosen. It also enables to some
49 extent the change of solution surrounding the sample, and it can be coupled to other techniques
50 like optical tweezers. However, it requires a complex dedicated setup: microscope,
51 micromanipulator, and precise control of the pressure in the aspiration tube¹⁵. The control of
52 the physico-chemical environment in real time requires several micromanipulators, and the
53 concentration of chemicals injected around the sample is non-homogeneous. Most importantly,
54 MPA suffers from very low throughput (~20 tests/h for single cells⁸, a few tests/h for vesicles,
55 and less than one test/h for cell aggregates¹⁵) since objects are intrinsically probed one by one,
56 which can be limiting due to the high sample-to-sample variability that is often typical of
57 biological systems.

58

59 Consequently, approaches to integrate micropipettes in microfluidic devices have been
60 proposed in the very last years. They target the above-mentioned limitations by designing
61 channels enabling parallel trapping and fluid control at the cell (or cell aggregate) scale. A
62 design relying on 3-level fabrication was developed ten years ago by Lee *et al.* for cells¹⁶, which
63 we improved in terms of alignment for the study of Giant Unilamellar Vesicles (GUV)¹⁷. Boot
64 *et al.* have recently adapted it to 3D cell aggregates¹⁸. While for this design microfluidics
65 permits automation of objects injection, the rectangular geometry has intrinsic limitations: a
66 quantitative analysis is complicated and some flow remains at the corner of the traps
67 constituting the pipette, even though recent work described the different regimes of clogging
68 rectangles with soft objects¹⁹. A 2-level design was used to probe the viscoelasticity of cell
69 nuclei in parallel thanks to constrictions²⁰, simpler to implement than the previous one but still
70 not fully quantitative. To relate the microscopic configuration to mechanical properties, 2D
71 geometries permitting optical access combined with rheological measurements were used to
72 characterize cell aggregate rearrangements²¹ or vesicle prototissues²², but their extension to
73 more realistic 3D tissues is far from obvious. Indeed, standard microfabrication techniques are
74 planar, which limits the possibility of properly integrating circular traps. 3D printing
75 technologies are associated with long writing time (several hours) for the resolution required
76 here, and can hardly ensure nanometric surface roughness needed to properly aspirate vesicles
77 or cell aggregates. As a way to eliminate the need for fluid confinement by surfaces, virtual
78 walls microfluidics has recently been demonstrated to characterize both cell and spheroid
79 mechanics²³, with quite a high throughput but limited to a global probing of objects.

80

81 Thus, a micropipette aspiration method, quantitative but with a higher throughput than classical
82 MPA, is still to be developed. We describe in this paper the SIMPA technology (sliding insert
83 micropipette aspiration) addressing the above-mentioned requirements, both at the scales of
84 vesicles and multicellular aggregates. It relies on the "sliding walls" proposed by Venzac *et*
85 *al.*²⁴, inserting sliding elements within PDMS chips. Here, rather than reconfigurability, which
86 was the strong point raised in²⁴, and which for instance permitted studying confined tissue
87 growth²⁵, we specifically exploited the particular microfabrication features of the approach.

This is the author's peer reviewed, accepted manuscript. However, the online version of record will be different from this version once it has been copyedited and typeset.

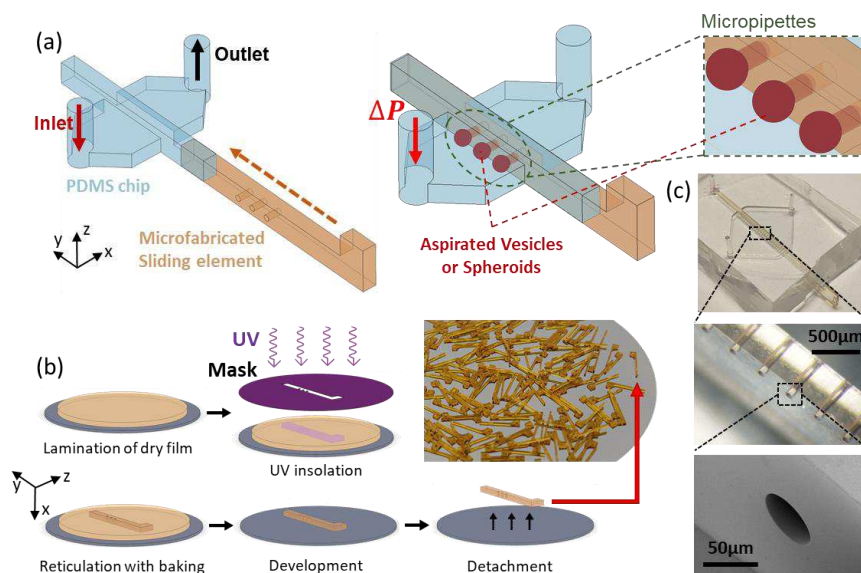
PLEASE CITE THIS ARTICLE AS DOI: 10.1063/1.5019333

88 Pipettes are designed and patterned by photolithography perpendicularly to the fabrication
 89 plane of the channel in which they are inserted (see Figure 1). In this way, the objects injected
 90 in a microchannel can be blocked by pipettes of a chosen shape: a circular cross-section permits
 91 quantitative measurements analyzed with classical models, since deformations occur like in
 92 standard MPA. Thanks to the integration, pipettes can be operated in parallel: we demonstrate
 93 it for 7 GUVs, and up to 23 spheroids. The throughput is thus multiplied by the number of
 94 pipettes in parallel when compared to classical MPA: with the SIMPA method we achieve ~10
 95 tests/h for GUV, and ~20 tests/h for spheroids.

96

97 In the following, we explain in the methods the design principles and fabrication technique of
 98 the chips, as well as their fluidic operation. We then demonstrate the interest of the technology
 99 by assessing two situations relevant to biophysics. First, we present the results obtained on
 100 vesicles: characterization of the elastic moduli of lipid bilayers with simple composition, and
 101 study of the influence of sugar and cholesterol on these moduli. Second, we detail the use of
 102 the devices for 3D cellular aggregates: measurements of the surface tension and viscoelastic
 103 characteristics, and study of the influence of molecules targeting cell-cell adhesion.

104



105

106 **Figure 1- Principle: On-chip pipettes integrated into a microfluidic chip thanks to sliding elements** - (a) Parts view: PDMS
 107 chip and sliding element. Assembled view after insertion, schematic close-up of aspirated micro-objects (Giant Unilamellar
 108 Vesicles or Spheroids). b) Microfabrication workflow of the sliding elements and photograph of dozens of them, manufactured
 109 in a single batch. c) Micrographs and SEM close-ups of the pipettes integrated into the sliding elements.

110

111

112

This is the author's peer reviewed, accepted manuscript. However, the online version of record will be different from this version once it has been copyedited and typeset.

PLEASE CITE THIS ARTICLE AS DOI: 10.1063/1.5019333

113 **Methods**

114 The microfluidic chips consisted of two parts, see Figure 1(a). Here, we explain the main
115 ingredients of its design, fabrication, and operation.

116 The first part is a PDMS chip, obtained by standard soft lithography. PDMS was cast and cured
117 on a two-level mold patterned in a photosensitive dry film (SU-8), preferred to liquid
118 photoresist since the thickness is as high as ~500 μm . After unmolding, holes were punched in
119 PDMS for fluidic access.

120 The first level of the mold corresponds to the main fluidic channel, see Figure 1(a). Its height
121 is slightly superior to the maximum diameter of the objects to be probed with pipettes, typically
122 ~100 μm for studies on vesicles, and ~450 μm for spheroids.

123 The fluidic configuration is quite simple with 1 input and 1 output, the channel just getting
124 wider at the location of sliding element insertion, to permit objects to be trapped in parallel.
125 Note however that the design can be complexified for additional functions: we demonstrate for
126 instance injection of a chemical stimulus around spheroids, thanks to extra lateral channels (see
127 Figure SI-8).

128 The fluidic channel is intersected by another guide, integrated in the second layer of the mold,
129 which is open to the outside. Its purpose is to accommodate the sliding element integrating the
130 pipettes, the second part that composes our chips.

131 The PDMS part was then bonded by plasma on a thin layer of PDMS (50 μm), compromising
132 between optical access for microscopy and deformation to avoid leakage.

133 The second element is the sliding element containing the pipettes to be integrated into the fluidic
134 channel by insertion in the PDMS chip. This long parallelepiped including holes that constitute
135 the pipettes was manufactured by photolithography using the same type of dry film, see Figure
136 1(b). After optimizing fabrication parameters, we obtained pipettes with an aspect ratio up to
137 20 (25 μm diameter for 500 μm length) and with a low roughness: typically, only a few ~20
138 nm-high asperities can be seen inside the pipette, as shown in Figure 1(c) and Figure SI-1. For
139 pipettes with lower diameters (down to 12 μm for GUVs, see Figure 2(a), and 5 μm for single
140 cells), a multi-layer lamination protocol was used. Lamination was realized on a sacrificial layer
141 (copper-titanium alloy), chemically etched after fabrication to release the sliding elements from
142 the wafer. Since fabrication was realized by batches on a 4-inch wafer, up to 150 reusable SMPs
143 (sliding micropipettes) could be obtained in a single fabrication run, which took a few hours.

144 Integration was made by inserting the SMP in the PDMS chip. This step could be achieved in
145 a few minutes, either manually under a binocular microscope, with alignment precision between
146 the pipettes and the fluidic channel in the order of 50 μm , or aided by a specific 3D-printed
147 holder if better alignment was required (see Figure SI-2). To reduce friction, an anti-adhesive
148 coating (fluorinated silane deposited in the gas phase) was realized on the SMPs before
149 insertion. Insertion was also facilitated thanks to isopropanol lubrication, eliminated afterward
150 by evaporation (see Supplementary Information).

151 Once inserted, the SMP blocked the fluid in the main channel by letting it flow only through its
152 cylindrical holes. The height and width of the guide were 20% smaller than the height and width
153 of the sliding element it received (typically 450 μm for the guide and 550 μm for the sliding
154 element), which we found optimum for elastic deformation to ensure a good sealing upon
155 insertion. We checked the absence of leakage in the whole range of the pressure controller (325
156 mbar). Thus, when a vesicle or a spheroid was injected into the inlet solution, it was carried by

157 the flow until it arrived in front of one of the micropipettes into which it was blocked and
 158 aspirated. In the design of the SMPs, the center of the pipette was placed at a Z position
 159 permitting objects to be trapped without touching the bottom of the fluidic channel, while being
 160 in focus under the microscope.

161 Chip operation differed slightly for GUVs and spheroids and are detailed in the next sections
 162 and the Supplementary Information. Fluidic protocols shared some characteristics: after
 163 degassing and injection of the buffer to pre-wet the whole chip, the solution containing the
 164 objects of interest was injected to trap them at the pipettes. Measurements of the mechanical
 165 properties were achieved by quantifying deformations (of the GUVs or spheroids) under a
 166 programmed pressure sequence, by optical microscopy and image analysis. Since the hydraulic
 167 resistance of the pipettes was much larger than those of the inlet and outlet channels, the
 168 pressure drop ΔP applied to vesicles or spheroids was almost equal to the pressure drop applied
 169 on the whole channel $\Delta P_{channel}$, even in the case where some pipettes were not blocked.

170 This fabrication approach permitted the integration of cylindrical holes (or any extruded shape
 171 of arbitrary cross-section) aligned with the main axis of fluidic channels, thanks to the
 172 photolithography of two elements along two orthogonal planes, which can hardly be achieved
 173 by standard manufacturing techniques. This feature makes SIMPA technology uniquely suited
 174 for high throughput micropipette aspiration, which we demonstrate in the following sections.

175

176 **Micropipettes for vesicles: elastic moduli of lipid membranes**

177 The mechanics of a lipid bilayer can be described by two main parameters: its resistance to
 178 bending, quantified by the bending modulus κ_c ; and its resistance to an increase of area per
 179 molecule (stretching modulus K_A). These moduli determine how the area of a vesicle A
 180 increases with its tension σ , with reference to a state at low tension A_0, σ_0 . The relative area
 181 increase, $\alpha = (A - A_0)/A_0$, reads ^{7,12}:

$$182 \quad \alpha = \frac{k_B T}{8\pi\kappa_c} \ln(1 + \sigma/\sigma_0) + (\sigma - \sigma_0)/K_A, \quad (1)$$

183 where k_B is the Boltzmann constant, and T the temperature.

184 The increase of area at low tension is mostly controlled by the smoothing of thermal fluctuations
 185 against bending (first term of equation (1)), whereas for a higher tension (typically 1 mN/m), it
 186 is set by the stretching modulus K_A (second term of equation (1)).

187 In standard micropipette experiments, a progressively increasing tension is induced thanks to a
 188 pressure difference ΔP applied to the vesicle aspirated in the pipette. With the hypothesis that
 189 the pressure inside the vesicle is equilibrated, and that the tension is homogeneous, the vesicle
 190 tension can be deduced from Laplace law according to:

$$191 \quad \sigma = \frac{\Delta P \cdot D_p}{4(1 - D_p/D_v)}, \quad (2)$$

192 where D_p and D_v are the pipette and vesicle diameters, respectively. With the additional
 193 hypothesis of constant vesicle volume during the experiment (low permeability of the lipid
 194 bilayer to solvent, few minutes experiments duration), and a first-order approximation
 195 ($D_p^2 \Delta L_p \ll D_v^3$), the area increase is deduced from ΔL_p , the position of the vesicle protrusion
 196 within the pipette with respect to the reference state (A_0, σ_0), see Figure 2(b):

$$197 \quad \Delta A = \pi D_p \Delta L_p \left(1 - \frac{D_p}{D_v}\right). \quad (3)$$

This is the author's peer reviewed, accepted manuscript. However, the online version of record will be different from this version once it has been copyedited and typeset.

PLEASE CITE THIS ARTICLE AS DOI: 10.1063/1.5019333

198 These principles apply to our microfluidic chips: we designed channels (100 μm deep, 400 μm
 199 wide) in which fluorescently labeled GUVs with a typical diameter of 50 μm , obtained by
 200 standard electroformation (see Supplementary Information), could flow. The channels
 201 integrated sliding elements with up to 7 pipettes of diameter $D_p \approx 12 \mu\text{m}$, see Figure 2(a). The
 202 pressure was slowly increased by steps (3 s duration), to quantify the increase of L_p with ΔP ,
 203 see Figure 2(b). The first step leading to a measurable GUV deformation was used as the
 204 reference state ($\Delta P_0, \Delta L_p = 0, A_0, \sigma_0$), see the top panel in Figure 2(b).

205 For large enough GUVs ($D_v \geq 2.5D_p$), standard image analysis was used to deduce ΔL_p as a
 206 function of ΔP . The relative area increase as a function of the tension was then calculated from
 207 Equations (2)-(3) for each GUV. The values of the bending and stretching moduli were then
 208 deduced by fitting Equation (1) to the experimental curve. As exemplified in Figure 2c showing
 209 six measurements realized in parallel, we have used a three-parameter fit, by letting the
 210 reference tension as a free parameter, in addition to the determination of κ_c and K_A . It was found
 211 to reproduce more accurately the data trend in the bending regime than a two-parameter fit and
 212 fixed experimental reference tension σ_{0exp} . The associated difference between σ_{0exp} and the
 213 fitted value was in the range $\delta\sigma_0 \leq 10^{-5} \text{ mN/m}$, corresponding to a pressure difference $\delta P \leq$
 214 3 Pa. We independently characterized the accuracy of pressure control to be better than 0.5 Pa,
 215 so this value is a little higher than expected. We attribute this slight discrepancy to higher
 216 uncertainty in determining the absolute value of the pressure, even though relative variations
 217 are precisely measured. With this procedure, the curve superimposed on experimental data both
 218 for bending and stretching regime, with a coefficient of determination of the fitting $R^2 \geq 0.99$.

219
 220
 221
 222
 223
 224
 225
 226
 227
 228

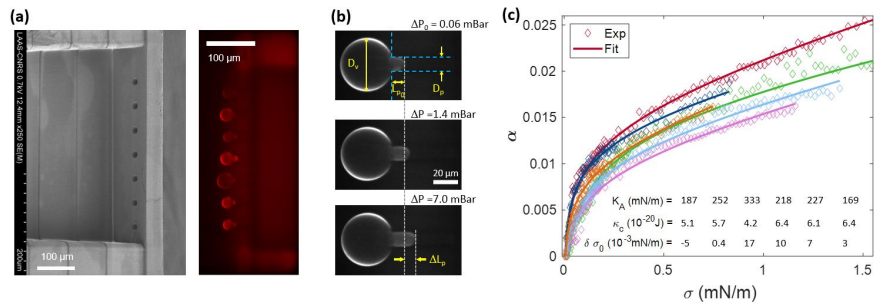


Figure 2- On-chip pipettes applied to Giant Unilamellar Vesicles to quantify the mechanics of lipid membranes (bending and stretching moduli). (a) SEM image of a sliding element with a design adapted to GUVs, including 7 pipettes (12 μm in diameter), and fluorescence microscopy micrograph of 7 DOPC GUVs trapped within such pipettes inserted in a PDMS channel. (b) Fluorescence micrographs of a GUV blocked inside a 12- μm -diameter pipette, for three values of the pressure difference applied to the vesicle. Reference situation ΔP_0 , and two successive equilibrium positions. The quasistatic increase of pressure causes a progressive increase of the GUV area, quantified from the length of the GUV protrusion within the pipette. (c) Evolution of the relative area increase as a function of the tension for six DOPC GUVs of the same experimental run, and fitted curve according to equation (1). The displayed numbers correspond to the outcomes of the fitting for this particular experiment, as a typical example of data dispersion.

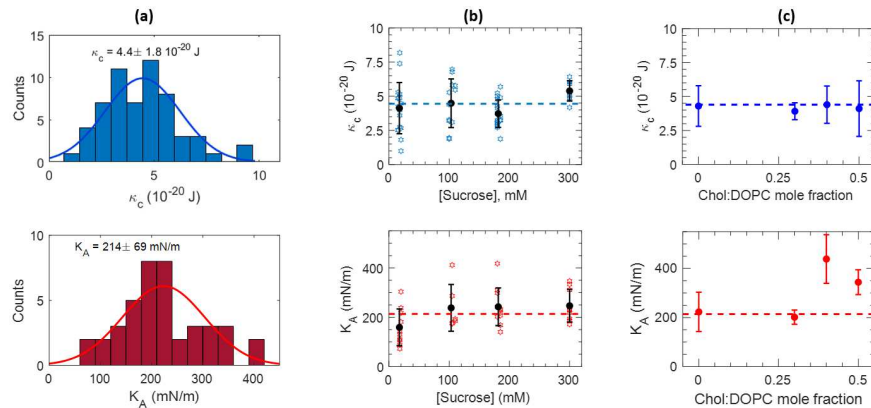
229 Results for GUVs of simple composition and effects of sugar and cholesterol

230 The results obtained with GUVs of simple composition (bilayer of the mono-unsaturated lipids
 231 1,2-dioleoyl-sn-glycero-3-phosphocholine, DOPC in sucrose solutions) are summarized in the
 232 histograms of Figure 3(a). The statistics are slightly lower for the stretching modulus K_A ($N =$
 233 41) than for the bending modulus κ_c ($N = 59$) because some GUVs escaped the pipettes at
 234 moderate pressure, without fully entering the stretching regime. We deduced the value of K_A
 235 only for vesicles escaping at a tension $\sigma \geq 0.75 \text{ mN/m}$. This fragility, which can be attributed

This is the author's peer reviewed, accepted manuscript. However, the online version of record will be different from this version once it has been copyedited and typeset.

PLEASE CITE THIS ARTICLE AS DOI: 10.1063/5.0193333

236 to dispersion in the lysis tension, possibly due to minor defects in some GUVs, was not
 237 correlated to the measured value of K_A and κ_c .
 238 We also investigated the effect of the sucrose concentration on the bilayer mechanics, for DOPC
 239 lipids, see Figure 3(b). No systematic variation of both bending and stretching moduli was
 240 observed from 15mM to 300 mM, within our experimental error.
 241 Finally, we performed measurements on bilayers composed of DOPC mixed with up to 50%
 242 cholesterol, Figure 3(c). We observed no dependence of the bending modulus on the
 243 cholesterol/lipid molar fraction, whereas the stretching modulus almost doubled for molar
 244 fractions 0.4 and 0.5.



245
 246 Figure 3- Bending and stretching moduli of lipid bilayers. (a) Histograms of the bending (top) and stretching (bottom) moduli
 247 of DOPC membranes, and associated Gaussian fits. (b) Influence of the sucrose concentration on the value of the bending (top)
 248 and stretching (bottom) moduli, for DOPC membranes. (c) Influence of cholesterol on the bending (top) and stretching (bottom)
 249 moduli of mixed DOPC-cholesterol vesicles, as a function of the cholesterol:DOPC mole fraction.

250 *Discussion: on-chip pipette to characterize vesicle mechanics*

251 Overall, the results in Figure 2 and Figure 3 show that the proposed approach is suited to
 252 determine the mechanical properties of lipid membranes, similar to the classical micropipette
 253 aspiration. However, the throughput of our method is higher (roughly multiplied by the number
 254 of pipettes in parallel, 7 in Figure 2) since several GUVs can be characterized in parallel. The
 255 integration in a microfluidic device has also the advantage of avoiding the manual search of
 256 vesicle and micromanipulation of the pipette, since the driving flow in the channel naturally
 257 brings the vesicles to the pipettes, and facilitates the trapping of GUVs. In addition, pressure
 258 controllers used in routine microfluidic setups have sub-second response time and permit the
 259 automation of pressure vs. time protocols.

260 The obtained values are reasonably consistent with the literature. For DOPC at room
 261 temperature, the determined stretching modulus $K_A = 214 \pm 69$ mN/m falls within the range
 262 of most micropipette measurements (respectively $K_A = 210 \pm 25$ mN/m, 198 mN/
 263 m, and 265 ± 18 mN/m for references ²⁶⁻²⁸). The bending modulus we obtained ($\kappa_c =$
 264 $4,4 \pm 1.8 \cdot 10^{-20}$ J) is in the lower limit of published values for measurements with
 265 micropipettes (respectively $\kappa_c \sim 9.1 \pm 1.5 \cdot 10^{-20}$ J, $8.5 \cdot 10^{-20}$ J, $4.7 \cdot 10^{-20}$ J for DOPC in
 266 references ^{26,28,29}), reported in a recent review ³⁰ to be in the range $\kappa_c = 4 - 16 \cdot 10^{-20}$ J for
 267 monounsaturated lipids. It has to be mentioned that systematic differences between groups and

This is the author's peer reviewed, accepted manuscript. However, the online version of record will be different from this version once it has been copyedited and typeset.

PLEASE CITE THIS ARTICLE AS DOI: 10.1063/1.5019333

268 measurement method are thoroughly discussed, and only partly explained by differences in the
269 probes scales or experimental protocols, in several reviews^{7,30-32}.

270 The dispersion of our data is a bit higher than in the literature (coefficients of variation 41%
271 and 29% for κ_c and K_A respectively). GUVs synthesized via electroformation have inherent
272 variability. We also attribute the dispersion to the fact that the only eliminated GUVs were those
273 with diameter $D_v \leq 2.5D_p$), or with visible defects (such as internal vesicles), contrary to
274 standard micropipette aspiration where the operator arbitrarily chooses the GUV to be probed.

275 The absence of influence of sugar concentration we observed (Figure 3(b)) is consistent with
276 most recent observations and discussions of the literature, even though this is still a quite
277 controversial issue.³²⁻³⁵

278 When varying the membrane composition by mixing DOPC with cholesterol, we observed no
279 change in the bending modulus, from pure DOPC up to the maximum cholesterol content tested
280 (0.5mol/mol). On the opposite, a two-fold increase was observed for K_A for increasing
281 cholesterol content, with a possible threshold between 0.3 and 0.4 molar fraction in cholesterol.
282 These observations complete a rich literature on the issue of cholesterol's influence on
283 membrane structure and properties. Bending rigidity was shown to be strongly lipid
284 dependent^{36,37}, stiffening by cholesterol being observed only for saturated lipids, with no effect
285 for mono-unsaturated lipids such as the DOPC used in the present study^{38,39}, or even slight
286 softening related to coupling between bending and cholesterol localization⁴⁰.

287 Finally, changing the chip design permits controlling physico-chemical stimuli around trapped
288 objects. Pipettes including slits to let a fraction of the flow pass can be used to probe vesicles
289 while submitted to shear stress: by using cross-shaped pipettes, we have observed that shear
290 stress affects lipid domains, as demonstrated in reference⁴¹, see Figure SI-7. Since a
291 microfluidic lateral channel can be integrated into the design, the approach is well-suited for
292 temporal change of the chemical environment surrounding the GUVs. It opens interesting
293 perspectives to investigate for example the kinetics of the interaction of lipid bilayers with
294 biomolecules or relevant synthetic entities (molecules, macromolecules, or nanosystems).

295

296 **Micropipettes on cell aggregates: quantifying spheroids' rheology**

297 Many biological tissues behave as viscoelastic fluids, which is both due to the properties of
298 individual cells (cytoskeleton, nucleus), and to the way they assemble in the tissue (extracellular
299 matrix, adhesion between cells). Thus, when a spheroid (simple 3D cell aggregate) is probed
300 by micropipette aspiration with a pressure step, it reacts with two different regimes. First, an
301 instantaneous deformation is observed, directly linked to the tissue's elastic properties. Then,
302 over time, the tissue flows into the micropipette like a viscous fluid. Several viscoelastic models
303 describe this type of material, but the modified Kelvin-Voigt shown in the insert of Figure 4(b)
304 is the simplest that closely reproduces the response observed in Figure 4(b). It consists of a
305 Kelvin-Voigt element (spring k_1 in parallel with damper μ_c), modified by the spring k_2 to
306 account for an instantaneous elastic response, in series with a dashpot μ_t , which corresponds to
307 long-term viscous flow. In this description of the tissue as a soft material, viscosity and
308 elasticity are completed by the aggregate's surface tension γ , excess of surface energy that
309 originates from a combination of the interaction between cells, and differences in cortical
310 tension between the peripheric and the core cells^{10,42}. In a standard micropipette experiment, a
311 spheroid of radius R is aspirated in a pipette of radius R_p with a suction pressure ΔP . The
312 effective force inducing spheroid deformation reads: $f = \pi R_p^2(\Delta P - \Delta P_c)$, where $\Delta P_c =$

313 $2\gamma\left(\frac{1}{R_p} - \frac{1}{R}\right)$ is the Laplace pressure generated by the curvature imposed by the pipette. ΔP_c
 314 corresponds to the minimum pressure needed for the spheroid to continuously flow inside the
 315 pipette. For $\Delta P > \Delta P_c$, the spheroid's response to a differential pressure step can be written, in
 316 terms of its temporal elongation $L(t)$ inside the pipette (see Figure 4(a)):

$$317 \quad L(t) = \frac{f}{k_1} \left(1 - \frac{k_2}{k_1 + k_2} e^{-\frac{t}{\tau_c}} \right) + \frac{f}{\mu_t} t, \quad (4)$$

318 where $\tau_c = \frac{\mu_c(k_1 + k_2)}{k_1 k_2}$ is a viscoelastic characteristic time.

319 The first term in equation (4) refers to a viscoelastic solid, with two elastic moduli acting at two
 320 timescales: a first modulus $E_i = (k_1 + k_2)/\pi R_p$, associated with an instantaneous deformation
 321 of the spheroid, and a second elastic modulus $E = k_1/\pi R_p$, which comes into play after a
 322 typical time τ_c . These two elastic moduli are usually attributed to the cellular cytoskeleton's
 323 reaction to pressure: the elasticity of the actin cortex is first assessed, fibers then rearrange,
 324 leading to a softer long-time elastic response.

325 The second term describes flow at the tissue level and it corresponds to the constant speed flow
 326 of a fluid of viscosity $\eta = \mu_t/3\pi^2 R_p$ inside the pipette, with the hypothesis that viscous
 327 dissipation occurs only at the inlet, due to cell rearrangements. As detailed in reference ¹⁴, this
 328 regime neglects wall friction, which is achieved thanks to surface treatment limiting cell
 329 adhesion on the pipette's walls.

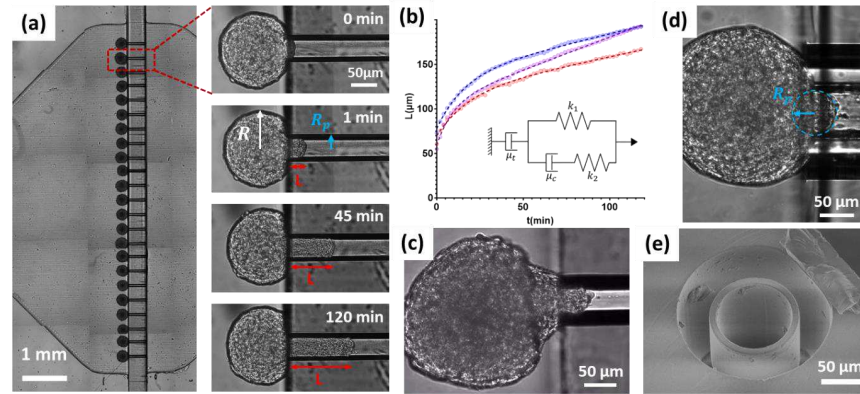
330 It is worth noting that these quantitative relationships between the Kelvin-Voigt parameters
 331 (k_1, k_2, μ_t) and the macroscopic viscoelastic moduli (E_i, E, η) slightly depends on the thickness
 332 of the pipette wall. They are correct for our SIMPA configuration (thick walls), whereas they
 333 need to be corrected by a few percent for classical MPA (thin walls), as discussed in references
 334 ⁴³ and ⁴⁴ regarding elasticity and viscosity, respectively.

335 We have developed microfluidic chips enabling parallel aspiration of up to 23 spheroids, see
 336 Figure 4(a). The channel height was 450 μm to accommodate all spheroid sizes. The chamber
 337 width was 10 mm for the 23-position chip (2 mm for the 5-position chip). A single
 338 microfabrication run allowed us to manufacture around 150 SMPs, see photo in Figure 1(b),
 339 which permitted us to test different pipette diameters and designs. Most experiments were
 340 conducted with 70 μm diameter pipettes, chosen as a compromise: much smaller than spheroids
 341 size, and significantly larger than cells size, for the granular nature of the tissue not to be too
 342 critical for the continuous description of the rheological model. Pipettes were 500 μm in length.
 343 A pressure step was applied to the spheroids, as detailed in the Supplementary Information. As
 344 mentioned in the Methods, the total channel pressure drop would be exerted on the pipettes
 345 even without spheroids blocking all of them, because they dominate the chip's hydraulic
 346 resistance. However, we only conducted experiments in which one spheroid is present in each
 347 pipette, to avoid the flow of buffer in free pipettes, that could affect the overall pressure
 348 difference because of a hydrostatic contribution upon increase of the outlet reservoir level.

This is the author's peer reviewed, accepted manuscript. However, the online version of record will be different from this version once it has been copyedited and typeset.

PLEASE CITE THIS ARTICLE AS DOI: 10.1063/5.0193333

349
350
351
352
353
354
355
356
357



358
359
360
361
362
363
364
365
366
367
368
369

370
371
372
373
374
375

376
377
378
379
380
381
382
383

Figure 4- On-chip pipettes applied to 3D cellular aggregates to quantify their viscosity and elasticity. (a) Micrograph of 23 spheroids trapped in the pipettes in the SIMPA chip. Close-up on a single micropipette: time-lapse of the aspiration of one A338 spheroid submitted to a pressure step $\Delta P = 50$ mbar from $t = 0$ s. (b) Evolution of the spheroids' positions $L(t)$ in the pipette as a function of time for 3 simultaneous parallel measurements, and fitted curves according to equation (4). (c) Micrograph of a spheroid just after release of the aspiration pressure. The conical shape indicates that Laplace pressure is not the only process expelling the spheroid from the pipette, during retraction. (d) Micrograph of a spheroid aspirated with a pressure just equal to the Laplace pressure ΔP_c , leading to a radius equal to the pipette's radius. (e) SEM image of the pipette design with a thin wall, used to improve the optical quality of the image in (d).

To validate quantitatively the SIMPA approach with respect to MPA, we performed measurements on the murine sarcoma cell line S180-GFP that was characterized by Guevorkian *et al.*¹³ by MPA. Since Laplace pressure contributes to the spheroid's flow (see Equation (4)), the surface tension γ needs to be determined to deduce the viscoelastic parameters. Like in reference¹³, aspiration was followed by retraction experiments, in which Laplace pressure is the only source of movement. The histograms of measured viscoelastic parameters are plotted in Figure SI-4 ($N = 23$). We obtained $\gamma = 10.8 \pm 2.4$ mN/m, $\eta = 1.37 \pm 0.03 \cdot 10^5$ Pa. s, $E = 213 \pm 17$ Pa, $E_i = 773 \pm 47$ Pa. The values of the viscosity and long-time elasticity are fully consistent with the results reported in reference¹³ ($\eta = 1.9 \pm 0.3 \cdot 10^5$ Pa. s, elastic modulus deduced from an average of relaxation times: $E = 700 \pm 100$ Pa), given that the cell line may have slightly evolved since 2010, and more importantly that the culture conditions to form the spheroids were not exactly the same in the two studies.

For A338 mouse pancreatic cancer cell spheroids, a typical timelapse for one position is shown on the right panel of Figure 4(a), and in Supplementary Video 1. The position of the spheroid protrusion as a function of time $L(t)$ was determined by a custom image segmentation algorithm described in Supplementary Information, see Figure SI-5 and Supplementary Video 3. Typical results of a single experiment driven on A338 spheroids are displayed in Figure 4(b), together with the fit of these results by equation (4).

However, regarding surface tension, we observed for this cell line a complex conical shape of the spheroid upon retraction, see Figure 4(c) and Supplementary Video 2, and its fast ejection from the pipette. Several mechanisms could explain this behavior: stored elastic energy could contribute to expelling the spheroid out of the pipette (similarly to what is mentioned in reference¹⁸), and additionally thanks to low wall friction the spheroid could slide upstream without dissipation and progressively round up at the pipette's corner because of surface tension. We thus used alternatives to such retraction experiments and measured γ by directly characterizing Laplace pressure thanks to other sets of experiments. We quantified the

384 minimum critical pressure leading to continuous flow of the spheroid ΔP_{crit} , which should also
 385 correspond to the pressure for which the radius of the spheroid meniscus (formed by cells at its
 386 surface within the pipette) equals the pipette radius, see Figure 4(d). This set of experiments
 387 was realized on a specially designed thin-wall pipette, see Figure 4(e), to improve the quality
 388 of optics. Both pressures were determined to be very close and equal to $\Delta P_{c-crit} = 5 \pm$
 389 0.5 mbar). These measurements led to a value of the surface tension $\gamma_{crit} = 10 \pm 1$ mN/m.
 390 We also quantified the ratio γ/η from the dynamics of spheroid fusion⁴⁵, see Supplementary
 391 Information, Figure SI-6. These independent off-chip experiments led to $\gamma_{fusion} = 4.5 \pm$
 392 0.9 mN/m. The fusion experiment mainly probes the external layers of the spheroid, and the
 393 surface tension of cell aggregates was recently discussed theoretically to be a multi-scale
 394 complex concept⁴⁶, so that different configurations could lead to slightly different results. The
 395 viscosity retained for this fitting was the one deduced from aspiration experiments. In addition,
 396 note that in both cases, the value corresponds to the surface tension at low stress, referred to as
 397 γ_0 in previous studies which have evidenced a possible increase of γ upon aspiration¹³. We
 398 finally retained the on-chip measured value γ_{crit} , since it was determined in the same flow
 399 configuration as the pipette aspiration. It is in the typical range of literature measurement of
 400 biological tissues' surface tension⁴⁷, even though most available data are on less cohesive
 401 configurations than the epithelial one probed here. Let us mention that since the applied
 402 pressure in aspiration experiments was significantly higher than the typical Laplace pressure,
 403 an error in surface tension determination would not critically affect the determination of
 404 viscoelastic parameters.

405 With this value of the surface tension, we extracted the rheological parameters from the fitting
 406 of the experimental curves $L(t)$ with equation (4), see Figure 4(b). The fittings closely
 407 reproduced the trends of the experiments. Graphically, tissue viscosity is deduced from the
 408 slope at a long time, whereas the first (short-time) elastic modulus E_i can be deduced from the
 409 initial instantaneous elongation of the spheroid, the second modulus E from the intercept of the
 410 long-time linear flow regime with the vertical axis, and τ_c from the typical time scale to reach
 411 this regime.

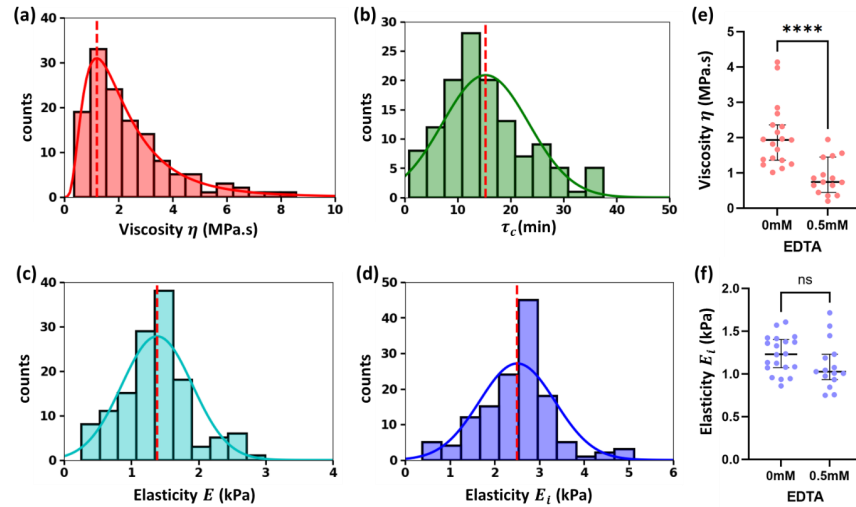
412

413 *Measuring viscoelastic properties of spheroids: results and discussion.*

414 The results obtained with A338 spheroids are shown in Figure 5(a). All ($N = 134$)
 415 measurements were realized with the 5-pipettes design, in about 30 experiments, each lasting a
 416 few hours, which demonstrates the high throughput of the method. We measured elastic moduli
 417 $E = 1.4 \pm 0.5$ kPa, $E_i = 2.5 \pm 0.9$ kPa, and a time scale $\tau_c = 15.3 \pm 8.1$ min (error bars
 418 indicates the standard deviation). For viscosity, the distribution was observed to be better fitted
 419 by a log-normal distribution than by a Gaussian. The maximum (mode) of the fitted distribution
 420 was $\eta_{ln} = 1.20$ MPa.s, with a distribution width $\sigma_{\eta-ln} = 0,67$ MPa.s. We observed a more
 421 reduced dispersion between spheroids of the same batch: the average of standard deviations
 422 deduced from single experiments (5 or 23 simultaneous measurements) was $\sigma_{\eta-batch} =$
 423 0.5 MPa.s and $\sigma_{E_i-batch} = 0.35$ kPa for the viscosity and short-time elasticity E_i respectively.
 424 These values can be interpreted as an upper bound of the measurement uncertainty,
 425 demonstrating the reproducibility of the technique. The width of the histograms in Figure 5(a)
 426 mostly originates from biological variability.

This is the author's peer reviewed, accepted manuscript. However, the online version of record will be different from this version once it has been copyedited and typeset.

PLEASE CITE THIS ARTICLE AS DOI: 10.1063/5.0193333



427
428
429
430

Figure 5- Viscoelastic properties of A338 cellular aggregates: histograms of the viscosity (a), characteristic viscoelastic time (b), long-time elasticity (c), short-time elasticity (d). (e-f) Influence of EDTA on the spheroids' viscosity and short-time elasticity.

431
432
433
434

To the best of our knowledge, no viscoelastic measurements have been published for this cell line. However, the high value of viscosity and elasticity, about ten times the typical values measured for very dynamic embryonic tissues⁴⁸, are consistent with the strong cohesion of pancreatic epithelial-like tissues.

435
436
437
438
439
440
441
442

We also assessed the effect of Ethylenediaminetetraacetic acid (EDTA). EDTA affects adhesion between cells by chelating metallic ions, including calcium, necessary for adhesion proteins to operate. We incubated the cells with EDTA during the formation of the spheroids before measuring viscoelastic properties. The results are shown in Figure 5(e-f). The viscosity was significantly reduced for spheroids incubated with EDTA with respect to the control, whereas short-time elasticity was not affected. This behavior is consistent with a reduced adhesion facilitating rearrangement of cells (T4 events²¹), leading to decreased viscosity, whereas elasticity, originating mostly from cells' cytoskeletons, was not strongly impacted.

443
444

We now discuss the specificities of the SIMPA technology for spheroid rheology, with respect to existing methods.

445
446
447
448
449
450
451
452
453
454

First, the approach benefits from the advantages of standard MPA: it is quantitative, and it probes optically determined locations of an object, which opens the possibility to test different zones of a tissue for non-spherical aggregate. MPA applies forces from the external cell layers, which can give complementary information to methods applying homogeneous stress, like magnetic rheometry⁴⁹. In our chips, since it is the microfluidic flow that pushes the spheroids towards the pipettes, the spheroid's orientation and the precise point they contact the pipette's inlet cannot be controlled by the operator independently of the fluidic design, which can appear as a limitation. However, for non-spherical objects it could turn into an advantage: the shape of the upstream channel and the location of pipettes on the sliding element could be specifically designed to set this orientation and probe well-defined areas.

This is the author's peer reviewed, accepted manuscript. However, the online version of record will be different from this version once it has been copyedited and typeset.

PLEASE CITE THIS ARTICLE AS DOI: 10.1063/1.5019333

455 The SIMPA technology has unique features compared to standard MPA: the throughput is
 456 multiplied by the number of spheroids that can be probed in parallel (demonstrated to be up to
 457 23 in this article). In addition, the chip format permits the use of low volumes of sample
 458 (typically a few hundred μL), with a spontaneous spheroid loading since the flow naturally
 459 pushes the spheroids to the free SMPs. The chips can also be washed and reused, and the
 460 spheroids extracted out of the chip for further characterization. It is possible to keep spheroids
 461 for long times (we observed spheroids stable for three days with no visible necrosis). This
 462 comes from the environmental chamber surrounding the chip on the microscope (temperature
 463 set to 37°C and 5% CO_2), but also from PDMS permeability to oxygen, and from a fast diffusion
 464 of nutrients within the chips. Finally, adding lateral fluidic channels close to the sliding element
 465 permits changing in real time the chemical environment of trapped spheroids, see Figure SI-8.
 466 As a proof of concept, we demonstrated the dynamic exposure of trapped spheroids to
 467 microparticles, see Supplementary Videos 4 and 5. This type of design could be relevant to
 468 study the response to drugs at short timescales, typically seconds or minutes. Quantifying the
 469 influence of different drugs, at different timescales, should improve our understanding of the
 470 microscopic origin of tissue rheology. In the same perspective, the technology can apply a
 471 dynamic pressure stimulus, as in reference ⁴⁹, which is a relevant way to assess the validity of
 472 different rheological models, or to apply spatio-temporal stimulations such as the ones
 473 originating from heart beating or circadian cycle.

474

475 **Conclusion**

476 We present in this paper the SIMPA technology, a parallel, quantitative integrated aspiration
 477 micropipette method. We demonstrate its relevance to characterize quantitatively mechanics
 478 both at the cell membrane scale and at the multicellular scale. With respect to standard MPA,
 479 its throughput is multiplied by the number of pipettes in parallel, shown to be for this proof of
 480 concept 7 and 23 for GUVs and spheroids respectively, leading to a throughput of order ~ 10
 481 tests/h for GUVs, and ~ 20 tests/h for spheroids. With respect to other integrated on-chip
 482 micropipettes^{18,20,21}, our approach is the only one that combines circular geometry and parallel
 483 probing, in a user-friendly format. Thus, even if interesting analyses have been developed
 484 recently for squares or rectangles¹⁹, circular traps are quantitative by design, they fully eliminate
 485 both anisotropy of the constraints and residual flows in the corners.

486 Several perspectives emerge from the versatility of the method, related to fluidic design. As the
 487 most obvious evolution, larger fluidic chambers, or pipettes placed at different z-positions,
 488 could lead to an even larger throughput by adding further parallel pipettes, if required. More
 489 interestingly, changing the chip design permits controlling physico-chemical stimuli around
 490 trapped objects.

491 As a further perspective, we could extend the single vesicle configuration to the probing of
 492 single cells, by using pipettes with diameters of order $2\text{-}5\ \mu\text{m}$, which is fully compatible with
 493 photolithography techniques used in this work. By providing direct measurements of
 494 mechanical parameters, with a better throughput than conventional micropipettes, that could be
 495 very complementary to high throughput microfluidic deformability cytometry⁵⁰.

496 Finally, specific versions of the technology can be developed to improve the quality of optics
 497 (thinner walls, see Figure 4(c), or glass versions of the sliding elements, see Supplementary
 498 Video 6). Overall, the SIMPA technology will help identify how collective properties emerge
 499 from individual cell deformations and rearrangements.

500 **Supplementary Material**

501 Supplementary material accompanies the manuscript on the APL Bioengineering website. It
 502 details microfabrication protocols, preparation of GUVS, cell culture and preparation of
 503 spheroids, and microfluidic protocols. SEM images of the pipettes are also provided (Figure SI-
 504 1), as well as the device to control the insertion of the pipettes (Figure SI-2), and
 505 characterization of the dry film fluorescence (Figure SI-3). Full histograms of the viscoelastic
 506 properties are shown in Figure SI-4. Image analysis algorithm is described and exemplified in
 507 Figure SI-5. The independent off-chip measurement of surface tension is explained and shown
 508 in Figure SI-6. An alternative geometry enabling to expose trapped object to a fluid shear stress
 509 is shown in Figure SI-7, together with its use to demonstrate the effect of shear on lipid domains.
 510 Figure SI-8 shows a second alternative geometry to control the chemical microenvironment
 511 around trapped objects. Finally, six supplementary videos are included, to exemplify the
 512 different steps and possibilities of the pipettes. Their legends are provided at the end of the
 513 Supplementary Material text.

514

515 **Data availability**

516 The data that support the findings of this study are available from the corresponding author
 517 upon reasonable request.

518

519 **References**

- 520 1. Diz-Muñoz, A., Weiner, O. D. & Fletcher, D. A. In pursuit of the mechanics that shape cell
 521 surfaces. *Nat. Phys.* **14**, 648–652 (2018).
 522 2. Petridou, N. I. & Heisenberg, C.-P. Tissue rheology in embryonic organization. *EMBO J.*
 523 **38**, e102497 (2019).
 524 3. Lenne, P.-F. & Trivedi, V. Sculpting tissues by phase transitions. *Nat. Commun.* **13**, 664
 525 (2022).
 526 4. Oswald, L., Grosser, S., Smith, D. M. & Käs, J. A. Jamming transitions in cancer. *J. Phys.*
 527 *Appl. Phys.* **50**, 483001 (2017).
 528 5. Deptuła, P. *et al.* Tissue Rheology as a Possible Complementary Procedure to Advance
 529 Histological Diagnosis of Colon Cancer. *ACS Biomater. Sci. Eng.* **6**, 5620–5631 (2020).
 530 6. Gottheil, P. *et al.* State of Cell Unjamming Correlates with Distant Metastasis in Cancer
 531 Patients. *Phys. Rev. X* **13**, 031003 (2023).
 532 7. Bassereau, P., Sorre, B. & Lévy, A. Bending lipid membranes: Experiments after W.
 533 Helfrich's model. *Adv. Colloid Interface Sci.* **208**, 47–57 (2014).
 534 8. González-Bermúdez, B., Guinea, G. V. & Plaza, G. R. Advances in Micropipette Aspiration:
 535 Applications in Cell Biomechanics, Models, and Extended Studies. *Biophys. J.* **116**, 587–
 536 594 (2019).
 537 9. Gonzalez-Rodriguez, D., Guevorkian, K., Douezan, S. & Brochard-Wyart, F. Soft Matter
 538 Models of Developing Tissues and Tumors. *Science* **338**, 910–917 (2012).
 539 10. Steinberg, M. S. Reconstruction of Tissues by Dissociated Cells. *Science* **141**, 401–408
 540 (1963).
 541 11. Chotard-Ghodsni, R. & Verdier, C. Rheology of Living Materials. in *Modeling of*
 542 *Biological Materials* (eds. Mollica, F., Preziosi, L. & Rajagopal, K. R.) 1–31 (Birkhäuser
 543 Boston, Boston, MA, 2007). doi:10.1007/978-0-8176-4411-6_1.
 544 12. Evans, E. & Rawicz, W. Entropy-driven tension and bending elasticity in condensed-
 545 fluid membranes. *Phys. Rev. Lett.* **64**, 2094–2097 (1990).

This is the author's peer reviewed, accepted manuscript. However, the online version of record will be different from this version once it has been copyedited and typeset.

PLEASE CITE THIS ARTICLE AS DOI: 10.1063/5.0193333

- 546 13. Guevorkian, K., Colbert, M.-J., Durth, M., Dufour, S. & Brochard-Wyart, F. Aspiration
547 of Biological Viscoelastic Drops. *Phys. Rev. Lett.* **104**, 218101 (2010).
548
549 14. Guevorkian, K., Brochard-Wyart, F. & Gonzalez-Rodriguez, D. Chapter eight - Flow
550 dynamics of 3D multicellular systems into capillaries. in *Viscoelasticity and Collective Cell*
551 *Migration* (eds. Pajic-Lijakovic, I. & Barriga, E. H.) 193–223 (Academic Press, 2021).
552 doi:10.1016/B978-0-12-820310-1.00008-2.
553 15. Guevorkian, K. & Maître, J.-L. Micropipette aspiration. in *Methods in Cell Biology* vol.
554 139 187–201 (Elsevier, 2017).
555 16. Lee, L. M. & Liu, A. P. A microfluidic pipette array for mechanophenotyping of cancer
556 cells and mechanical gating of mechanosensitive channels. *Lab. Chip* **15**, 264–273 (2014).
557 17. Elias, M. *et al.* Microfluidic characterization of biomimetic membrane mechanics with
558 an on-chip micropipette. *Micro Nano Eng.* **8**, 100064 (2020).
559 18. Boot, R. C. *et al.* High-throughput mechanophenotyping of multicellular spheroids
560 using a microfluidic micropipette aspiration chip. *Lab. Chip* **23**, 1768–1778 (2023).
561 19. Moore, C. P., Husson, J., Boudaoud, A., Amselem, G. & Baroud, C. N. Clogging of a
562 Rectangular Slit by a Spherical Soft Particle. *Phys. Rev. Lett.* **130**, 064001 (2023).
563 20. Davidson, P. M. *et al.* High-throughput microfluidic micropipette aspiration device to
564 probe time-scale dependent nuclear mechanics in intact cells. *Lab. Chip* **19**, 3652–3663
565 (2019).
566 21. Tlili, S. L., Graner, F. & Delanoë-Ayari, H. A microfluidic platform to investigate the
567 role of mechanical constraints on tissue reorganization. *Development* **149**, dev200774
568 (2022).
569 22. Layachi, M., Casas-Ferrer, L., Massiera, G. & Casanellas, L. Rheology of vesicle
570 prototissues: A microfluidic approach. *Front. Phys.* **10**, (2022).
571 23. Panhwar, M. H. *et al.* High-throughput cell and spheroid mechanics in virtual fluidic
572 channels. *Nat. Commun.* **11**, 2190 (2020).
573 24. Venzac, B. *et al.* Sliding walls: a new paradigm for fluidic actuation and protocol
574 implementation in microfluidics. *Microsyst. Nanoeng.* **6**, 1–10 (2020).
575 25. Meriem, Z. B. *et al.* A microfluidic mechano-chemostat for tissues and organisms
576 reveals that confined growth is accompanied with increased macromolecular crowding. *Lab.*
577 *Chip* (2023) doi:10.1039/D3LC00313B.
578 26. Lu, L., Doak, W. J., Schertzer, J. W. & Chiarot, P. R. Membrane mechanical properties
579 of synthetic asymmetric phospholipid vesicles. *Soft Matter* **12**, 7521–7528 (2016).
580 27. Chen, D. & Santore, M. M. Hybrid copolymer–phospholipid vesicles: phase separation
581 resembling mixed phospholipid lamellae, but with mechanical stability and control. *Soft*
582 *Matter* **11**, 2617–2626 (2015).
583 28. Rawicz, W., Olbrich, K. C., McIntosh, T., Needham, D. & Evans, E. Effect of Chain
584 Length and Unsaturation on Elasticity of Lipid Bilayers. *Biophys. J.* **79**, 328–339 (2000).
585 29. Shchelokovskyy, P., Tristram-Nagle, S. & Dimova, R. Effect of the HIV-1 fusion
586 peptide on the mechanical properties and leaflet coupling of lipid bilayers. *New J. Phys.* **13**,
587 025004 (2011).
588 30. Boichichio, D. & Monticelli, L. Chapter Five - The Membrane Bending Modulus in
589 Experiments and Simulations: A Puzzling Picture. in *Advances in Biomembranes and Lipid*
590 *Self-Assembly* (eds. Iglíč, A., Kulkarni, C. V. & Rappolt, M.) vol. 23 117–143 (Academic
591 Press, 2016).
592 31. Nagle, J. F. Introductory Lecture: Basic quantities in model biomembranes. *Faraday*
593 *Discuss.* **161**, 11–29 (2013).
594 32. Nagle, J. F., Jablin, M. S., Tristram-Nagle, S. & Akabori, K. What are the true values of
595 the bending modulus of simple lipid bilayers? *Chem. Phys. Lipids* **185**, 3–10 (2015).
596 33. Vitkova, V., Genova, J., Mitov, M. D. & Bivas, I. Sugars in the Aqueous Phase Change
597 the Mechanical Properties of Lipid Mono- and Bilayers. *Mol. Cryst. Liq. Cryst.* **449**, 95–106
598 (2006).

This is the author's peer reviewed, accepted manuscript. However, the online version of record will be different from this version once it has been copyedited and typeset.

PLEASE CITE THIS ARTICLE AS DOI: 10.1063/5.0193333

- 598 34. Nagle, J. F., Jablin, M. S. & Tristram-Nagle, S. Sugar does not affect the bending and
599 tilt moduli of simple lipid bilayers. *Chem. Phys. Lipids* **196**, 76–80 (2016).
600 35. Dimova, R. Recent developments in the field of bending rigidity measurements on
601 membranes. *Adv. Colloid Interface Sci.* **208**, 225–234 (2014).
602 36. Gracià, R. S., Bezlyepkina, N., Knorr, R. L., Lipowsky, R. & Dimova, R. Effect of
603 cholesterol on the rigidity of saturated and unsaturated membranes: fluctuation and
604 electrodeformation analysis of giant vesicles. *Soft Matter* **6**, 1472 (2010).
605 37. Eid, J., Razmazma, H., Jraij, A., Ebrahimi, A. & Monticelli, L. On Calculating the
606 Bending Modulus of Lipid Bilayer Membranes from Buckling Simulations. *J. Phys. Chem.*
607 *B* **124**, 6299–6311 (2020).
608 38. Nagle, J. F. *et al.* A needless but interesting controversy. *Proc. Natl. Acad. Sci.* **118**,
609 e2025011118 (2021).
610 39. Pan, J., Tristram-Nagle, S. & Nagle, J. F. Effect of cholesterol on structural and
611 mechanical properties of membranes depends on lipid chain saturation. *Phys. Rev. E* **80**,
612 021931 (2009).
613 40. Pöhl, M., Trollmann, M. F. W. & Böckmann, R. A. Nonuniversal impact of cholesterol
614 on membranes mobility, curvature sensing and elasticity. *Nat. Commun.* **14**, 8038 (2023).
615 41. Sturzenegger, F., Robinson, T., Hess, D. & Dittrich, P. S. Membranes under shear stress:
616 visualization of non-equilibrium domain patterns and domain fusion in a microfluidic device.
617 *Soft Matter* **12**, 5072–5076 (2016).
618 42. Manning, M. L., Foty, R. A., Steinberg, M. S., Schoetz, E.-M. & Honig, B. H. Coaction
619 of intercellular adhesion and cortical tension specifies tissue surface tension. *Proc. Natl.*
620 *Acad. Sci. U. S. A.* **107**, 12517–12522 (2010).
621 43. Aoki, T., Ohashi, T., Matsumoto, T. & Sato, M. The pipette aspiration applied to the
622 local stiffness measurement of soft tissues. *Ann. Biomed. Eng.* **25**, 581–587 (1997).
623 44. Dagan, Z., Weinbaum, S. & Pfeffer, R. An infinite-series solution for the creeping
624 motion through an orifice of finite length. *J. Fluid Mech.* **115**, 505 (1982).
625 45. Kosheleva, N. V. *et al.* Cell spheroid fusion: beyond liquid drops model. *Sci. Rep.* **10**,
626 12614 (2020).
627 46. Pajic-Lijakovic, I., Eftimie, R., Milivojevic, M. & Bordas, S. P. A. Multi-scale nature
628 of the tissue surface tension: Theoretical consideration on tissue model systems. *Adv. Colloid*
629 *Interface Sci.* **315**, 102902 (2023).
630 47. Foty, R. A., Forgacs, G., Pflieger, C. M. & Steinberg, M. S. Liquid properties of
631 embryonic tissues: Measurement of interfacial tensions. *Phys. Rev. Lett.* **72**, 2298–2301
632 (1994).
633 48. Forgacs, G., Foty, R. A., Shafir, Y. & Steinberg, M. S. Viscoelastic Properties of Living
634 Embryonic Tissues: a Quantitative Study. *Biophys. J.* **74**, 2227–2234 (1998).
635 49. Mary, G. *et al.* All-in-one rheometry and nonlinear rheology of multicellular aggregates.
636 *Phys. Rev. E* **105**, 054407 (2022).
637 50. Urbanska, M. *et al.* A comparison of microfluidic methods for high-throughput cell
638 deformability measurements. *Nat. Methods* **17**, 587–593 (2020).
639

640 Acknowledgements

641 This work was supported in part by CNRS through the PICS CNRS program “Microfluidics for
642 Soft Matter”, and by INSIS-CNRS. This work was partly supported by LAAS-CNRS micro
643 and nanotechnologies platform member of the French RENATECH network. BGB was
644 supported by a fellowship from the “Programa Propio de I+D+I 2022” of Universidad
645 Politécnica de Madrid. Funding by “ADI, Université de Toulouse, Région Occitanie”, and by
646 Federation Fermat, Université de Toulouse, are acknowledged. We thank Benjamin Reig for
647 SEM imaging, Sandrine Souleille for microfluidics experiments, Charline Blatché for cell

This is the author's peer reviewed, accepted manuscript. However, the online version of record will be different from this version once it has been copyedited and typeset.

PLEASE CITE THIS ARTICLE AS DOI: 10.1063/1.5019333

648 culture, and Julien Roul for help in microscopy experiments. We thank Karine Guevorkian and
649 Gregory Beaune for gently providing the S180 cell line.

650

651 **Author Contributions**

652 ME, HA, MP realized experiments on GUVs. SL, ME, PL realized experiments on spheroids.
653 SL and BGB realized experiments on single cells. SL, ME, PL, HA, MP, AL, FM, DB
654 contributed to chip fabrications. LM, JB calibrated the photolithography process. DB, CM, MD,
655 CR, PJ contributed to experiments and supervised the research. PJ and SL wrote a first draft of
656 the manuscript, all authors read and amended the manuscript.

657

658 **Competing interests**

659 There are no conflicts to declare.

660 Correspondence and requests for materials should be addressed to pierre.joseph@laas.fr.